RESEARCH ARTICLE

ADVANCED OPTICAL MATERIALS
www.advopticalmat.de

Size Effect on Photothermal Heating Ability of Gold Bipyramids

Aadesh Mohan Naik, Ana Sánchez-Iglesias, José Luis Montaño-Priede PhD, Nirmala Maria D'souza, Jordi Sancho-Parramon, Stefano A. Mezzasalma, Anish Rao, and Marek Grzelczak**

Gold nanoparticles (AuNPs) exhibit photothermal properties that are fundamental to biomedical and catalytic fields. However, the relationship between photothermal heating efficiency and nanoparticle characteristics often features a non-intuitive behavior, being dependent on experimental parameters, sample scale (microscopic versus macroscopic), and material phase (solid or liquid). Using gold bipyramids (AuBPs) as a model system and employing a combination of experimental and computational approaches, photothermal heating is investigated as a function of nanoparticle dimensions while maintaining comparable optical properties. The computational analysis revealed an inverse correlation between the achievable maximum temperature at the single-particle level versus multi-particle systems. At the macroscopic scale, it is observed that photothermal heating efficiency follows an inverse proportionality with nanoparticle volume, with notable deviations occurring at reduced nanoparticle sizes. This deviation suggests the emergence of additional energy relaxation pathways. To outline practical implications of these findings, processable agarose films containing AuBPs capable of enhancing the performance of light-powered Stirling engine are developed.

1. Introduction

The conversion of incident photons into heat was traditionally counted as a waste of energy, earning metals the reputation of being *lossy* plasmonic materials.[1,2] However, this perceived loss became an advantage when researchers began repurposing the so-called '*lost heat*' for innovative applications, including optical tweezing,[3] photothermal therapy,[4] photovoltaics,[5] thermoelectric devices,[6] as well as actuators and soft-robotic systems.[7] Applications emerging from such an inventive heat management have spearheaded research aimed at understanding the factors not only influencing but also maximizing photothermal heating efficiency of plasmonic NPs.[8] Central to this effort is the exploration of how size,[9,10] shape,[11–13] composition,[14] sample homogeneity,[15] and configuration of experimental setup (thermal camera,[9,10,16] transient absorption[17,18]) affect the evaluation of photothermal heating of plasmonic nanoparticles. Certainly, the initial breakthrough in experimental thermoplasmonics has been made by using spherical nanoparticles as a model system.[19] Increasing the size, however, inevitably induces a redshift in their localized surface plasmon resonance (LSPR), altering their interaction with incident light and complicating a systematic analysis of size-dependent effects. The rod-like shape is more convenient in testing the

A. M. Naik, A. Sánchez-Iglesias, J. L. Montaño-Priede, A. Rao, M. Grzelczak
Centro de Física de Materiales (CFM-MPC)
CSIC-UPV/EHU
Paseo Manuel de Lardizabal 5, Donostia - San Sebastián 20018, Spain
E-mail: anish.rao@csic.es; marek.g@csic.es

A. M. Naik
University of the Basque Country (UPV/EHU)
Donostia–San Sebastián 20080, Spain

The ORCID identification number(s) for the author(s) of this article can be found under https://doi.org/10.1002/adom.202501006

DOI: 10.1002/adom.202501006

N. M. D'souza
Institute of Physics
Bijenička cesta 46, Zagreb 10000, Croatia

J. Sancho-Parramon, S. A. Mezzasalma
Materials Physics Division
Laboratory of Optics and Optical Thin Films
Ruđer Bošković Institute
Bijenička cesta 54, Zagreb 10000, Croatia

S. A. Mezzasalma
Institute for advanced Neutron and X-ray Science (LINXS)
Lund University
IDEON Building: Delta 5, Scheelevägen 19, Lund 223 70, Sweden

M. Grzelczak
Donostia International Physics Center (DIPC)
Pase Manuel de Lardizabal 4, Donostia - San Sebastián 20018, Gipuzkoa, Spain

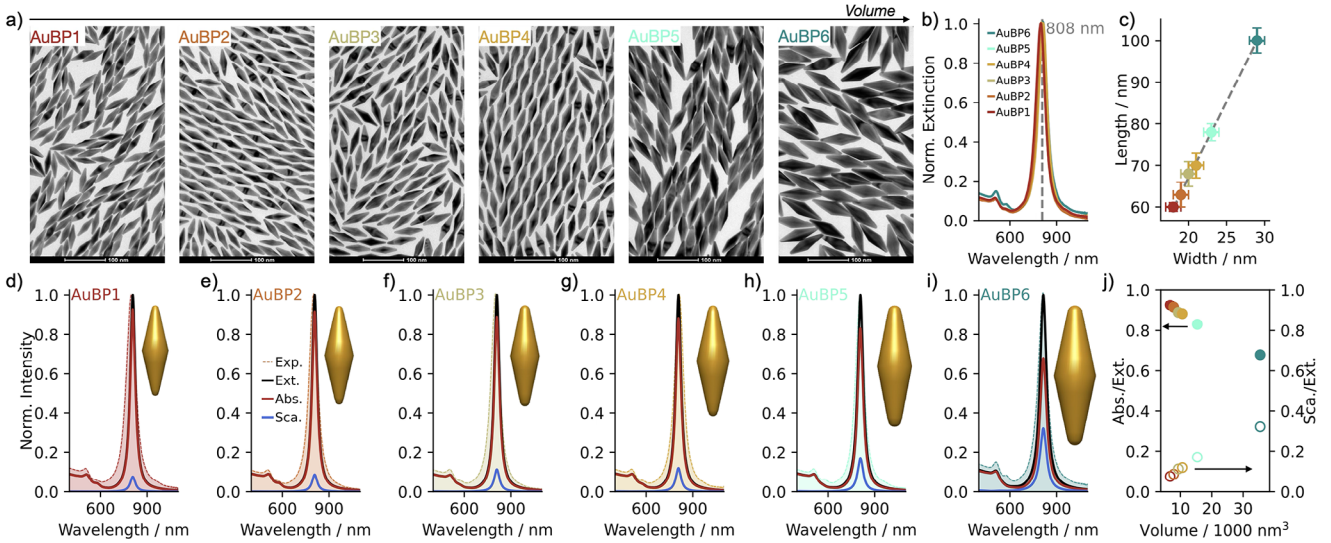

Figure 1. Gold Bipyramids. a) TEM images of AuBPs with increasing volume and constant aspect ratio. b) Normalized UV-Vis-NIR spectra of samples shown in a) displaying LSPR maxima located at ~808 nm. c) Length vs. width of the samples shown in a). Dashed line: linear fit. d–i) Numerical absorption, scattering and extinction cross-section spectra. The shaded regions represent the experimental UV-Vis-NIR spectra from b). Insets: 3D models used for the numerical calculations. j) Change in the absorption-to-extinction ratio (full circles) and scattering-to-extinction ratio (open circles) as a function of nanoparticles volume.

photothermal heating[9,10] since the LSPR position is more sensitive to the aspect ratio (length to width) rather than to their volume, offering a more straightforward pathway for disentangling size effects from LSPR shifts. An emerging type of plasmonic nanoparticles - gold bipyramids[20–22] - with demonstrated superior photothermal performance,[16,20,22] remains barely studied in the size-dependent photothermal efficiency. The recent progress in simplifying experimental protocol for these nanoparticles,[23,24] made it possible to fine-tune their volume at unaltered optical properties, rendering them an excellent platform for further evaluation and use of their photothermal properties.

This study evaluates the photothermal conversion efficiency of gold bipyramids and demonstrates their application in mechanical energy generation. Through numerical simulations, we showed that with increasing volume of AuBPs at a constant optical density, their heating ability follows opposite trends when interpreted on an individual or multi-particle levels. Specifically, macroscopic temperature changes are dominated by collective thermal effects rather than the intrinsic photothermal response of individual nanoparticles. Furthermore, while both experimental and computational results confirm an inverse relationship between AuBP volume and photothermal heating efficiency, deviations emerge at reduced nanoparticle dimensions. These anomalies suggest the activation of additional energy dissipation mechanisms, potentially involving non-radiative plasmonic decay or interfacial thermal effects. To translate our fundamental insights into practical applications, we engineered processable AuBPs-embedded agarose composites. These materials exhibit robust thermoplasmonic properties and enhance the performance of light-driven Stirling engines, showcasing their potential for solar-to-mechanical energy conversion. This work establishes a framework for repurposing low-grade thermal energy in plasmon-enhanced applications. Our findings highlight new opportunities for utilizing plasmonic nanoparticles in *waste-heat* recovery technologies through rational design of their optical properties.

2. Results and Discussion

2.1. Synthesis of Bipyramids

We commenced our study with the chemical synthesis of AuBPs samples with varying volume and invariant position of LSPR (**Figure 1**). In doing so, we utilized a protocol recently developed that involves two primary experimental parameters, namely, the concentration of cationic surfactants and Au seeds.[23,24] The seed concentrations controls the volumes of AuBPs, the concentration of cationic surfactant (cetyltrimethylammonium bromide, CTAB) governs the aspect ratio and thus the position of the maximum of LSPR in the resulting AuBPs (Sections S1.3 and S1.4, Table S1, Supporting Information). That is, the extinction spectra of all experimental samples showed a reasonable overlap sharing the maximum of LSPR position at 808 nm (Figure 1b). Note that the selection of 808 nm was constrained by the wavelength of continuous wave (CW) laser used as light source in the photothermal heating experiments. A visual

Table 1. Structural characterization of AuBPs.

Sample	Length [nm]	Width [nm]	Aspect Ratio	Volume [nm³]
AuBP1	60 ± 1	18 ± 1	3.3	6742
AuBP2	63 ± 3	19 ± 1	3.3	7872
AuBP3	68 ± 3	20 ± 1	3.4	9364
AuBP4	70 ± 3	21 ± 1	3.3	10629
AuBP5	78 ± 3	23 ± 1	3.4	15407
AuBP6	100 ± 3	29 ± 1	3.5	35431

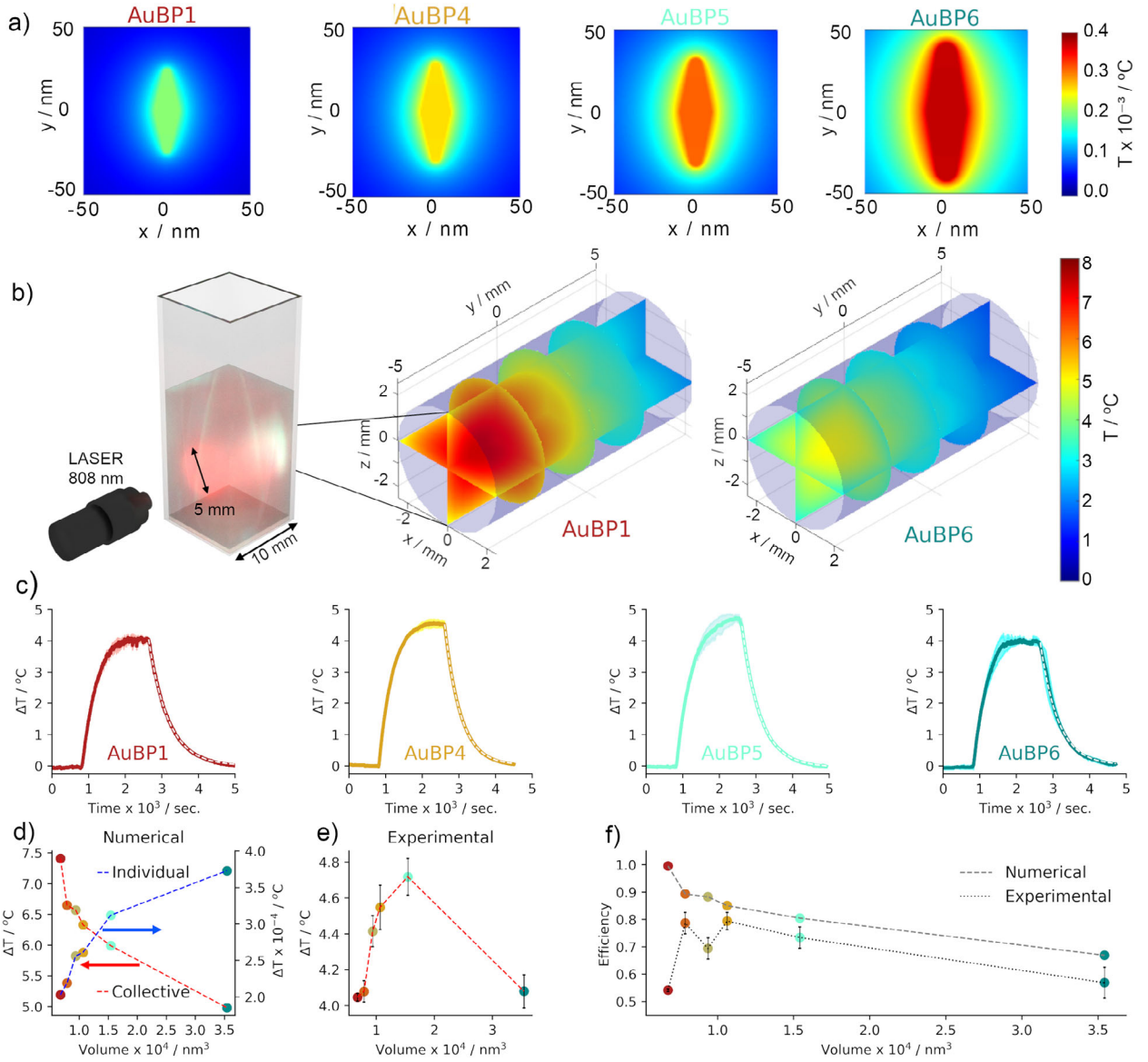

Figure 2. Photothermal heating. a) Computed temperature distribution within individual AuBPs, showing the temperature increase with increasing nanoparticle volume. b) Temperature increase in a cylindrical section of the cuvette under laser illumination at equilibrium (beam diameter 5 mm) for AuBP1 and AuBP6. Under collective heating regime, small volume AuBPs outperform larger AuBPs. c) Heating curves for all samples, with averages from three heating cycles shown in solid colors and standard deviations represented by faint shading. White dashed line: fit of exponential decay adopted to calculate photothermal efficiency. d) Numerical values of individual (gray dashed line) and collective (black dashed line) ΔT (max) as a function of AuBP volume. e) Experimental values of ΔT (max) as a function of AuBP volume. f) Experimental (solid line) and numerical (dashed line) values of heating efficiency as a function of AuBP volume.

inspection of Transmission Electron Microsocpy (TEM) micrographs confirmed the high-quality AuBPs with increasing volume from sample AuBP1 to sample AuBP6 (Figure 1a). Further analysis of TEM images (n>200 AuNPs) showed a proportional increase of length and width (Figure 1c). The slope of linear fit was 3.6, which is in reasonably good agreement with the mean values of the aspect ratio (3.4) obtained from image analysis for the entire set of samples (**Table 1**). The volume variation was 5.2-fold across the entire set of samples, as calculated by our recent method[25] (Section S1.6, Supporting Information; Table 1). Notably, the volume of AuBP1 was ~6742 nm^3, making it 3 times smaller than the smallest AuBP previously studied for photothermal heating in earlier research.[16] The as-prepared AuBPs were washed and stored in aqueous solution of cationic surfactant (cetyltrimethylammonium chloride, CTAC, 10 mM) for further studies.

It is commonly agreed that the performance of photothermal heating by individual AuNPs is dictated by their absorption cross-sections,[12] which in turn changes with their volume. That is, the smaller the volume of nanoparticles, the lower the relative contribution of the scattering cross-section. Therefore, we hypothesize that the AuBP1–6 samples should exhibit progressive

variations in the relative contributions of absorption and scattering to their total extinction spectrum. To test our hypothesis, we simulated the extinction, absorption, and scattering cross-sections using the Boundary Element Method approach,[26] which solves integro-differential equations derived from the boundary conditions on Maxwell's equations. The optical properties were calculated by assuming 3D models of AuBPs generated by a geometrical inversion method,[25] using literature values of refractive index for both gold[27] and water (1.333), and unpolarized incident light. As expected, optical spectra reveal a decrease in the absorption contribution and an increase in scattering as the volume of AuBPs increases (Figure 1d–i). Worth is mentioning the good agreement found between experimental and numerical spectra. The absorption-to-extinction ratio (Abs./Ext.) decreases and the scattering-to-extinction ratio (Scatt./Ext.) increases with particle volume (Figure 1j). For the smallest nanoparticles (AuBP1), light extinction is almost entirely due to absorption, whereas for the largest bipyramids (AuBP6), extinction consists of ~70% absorption and ~ 30% scattering. This reduction in absorption suggests that the photothermal performance of AuBPs is expected to decline in larger particles, as an increasing amount of light is scattered.

2.2. Thermal Properties

Prior to the experimental evaluation of the photothermal properties of AuBPs, we performed numerical simulations of heat transfer. The AuBPs are considered as a heat source with heat dissipation power per unit volume equal to the product of the laser irradiance and the particle absorption cross-section, as calculated from Maxwell's electromagnetic equations. The calculated temperature generated by the AuBPs and their surroundings increases with AuBP volumes (**Figure** 2a,d). The observed trend can be explained by the larger absorption cross-section of AuBPs with larger volume. In particular, the value of the absorption cross-section increases from 3086 to 9969 nm^2, for AuBP1 and AuBP6 respectively, even though the relative contribution of absorption to the extinction cross-section is inversely proportional to volume. However, as our experimental scenario involves a large number of nanoparticles, a collective thermal effect must be considered when analyzing heat transfer.[28] Thus, we modeled multi-particles system that approximates macroscopic dispersion (2 mL) containing nanoparticles arranged in a lattice-like configuration. Since the optical density (OD) across all samples was maintained constant, the nanoparticle density was systematically reduced from sample AuBP1 to AuBP6, resulting in the increase of interparticle distance. (Table S4, Supporting Information). The laser beam passing through the cuvette formed a cylinder with a diameter of 5 mm and a length of 10 mm (Figure 2b; Figure S2, Supporting Information). The volume of the cylinder is reasonably supposed to contain a homogeneous nanoparticle distribution (Section S7, Supporting Information for further details). The collective effect considered here assumes the existence of a steady-state, in which particles stay fixed at their positions, neglecting stirring and convective effects. Therefore, our model offers a qualitative rather than an exact thermodynamic description. Interestingly, collective effects reverse the temperature trend observed for single AuBPs (Figure 2d). The maximum temperatures observed from AuBP1 to AuBP6 were 7.41, 6.65, 6.57, 6.33, 5.99, and 4.98 °C, respectively (Figure 2d). It is reasonable to state that the larger values of the maximum temperature generated by the small AuBPs result from their greater number compared to large AuBPs, as the concentration of nanoparticles changes 5.2 times across the entire sample set from AuBP1 to AuBP6. Thus, the maximum temperatures in a multi-particle system are conditioned by the attenuation of light as it propagates through the dispersion, reducing the effective number of particles contributing to the temperature increase. Consequently, the largest temperatures in the system with fixed nanoparticle positions are found in the regions near the laser entry point in the cuvette (Figure 2b). In general, the maximum temperatures simulated here should be considered as a guide for estimating the upper limit for the available temperature in our experimental setup.

Next, we evaluated experimentally the photothermal properties of AuBPs. In a typical measurement, the temperature was monitored using a thermal camera placed orthogonally to the incident beam of a continuous wave (CW) laser (808 nm, ~677 mW cm^{-2}), which illuminated a PMMA cuvette containing AuBPs (2 mL, CTAC 10 mM, OD = 1 at 808 nm). Note that maintaining constant OD values implies a 5.2-fold change in nanoparticle density, where the decrease in dimensions increases the number of nanoparticles in solution. Nevertheless, keeping the concentration low (OD = 1) does not affect photothermal efficiency.[29] Continuous stirring ensured homogeneous temperature increase throughout the cuvette (Figure S2). Although the design of the optimal experimental setup for estimating photothermal efficiency remains a subject of debate,[8] our four-side cuvette setup meets the necessary standards, especially if overall trends instead of absolute values are pursued. Under illumination, the temperature saturated after 1200–1500 sec, followed by a drop when the laser was turned off after 1800 s (30 min) (Figure 2c). Heating and cooling cycles were repeated three times (see Figure S3, Supporting Information). Interestingly, the obtained maximum temperature increased from 4.0 to 4.7 °C upon decreasing nanoparticles volume, followed by its sudden drop to 4.1 °C for AuBP1 (Figure 2e). That is, the smallest and the larges nanoparticles rendered the same temperature rise, that is quite opposite to the numerical simulation as shown in Figure 2d. A feasible reason behind such a discrepancy are non-thermal relaxation pathways by the AuBPs of reduced volume and thermal inhomogeneity in the samples due to the increased total number of nanoparticles.[30] We can discard possible aggregation of the AuBPs during irradiation, as the optical characterization confirmed excellent colloidal and structural stability after three consecutive heating cycles (see Figure S4, Supporting Information).

To calculate heating efficiencies, we employed Roper's method,[31] in which temperature decays were fitted using an exponential decay function (Figure 2c - white dashed lines). Note that, to mitigate biased estimates of fitting parameters due to linearization,[32] we opted for non-linearized equations for the entire sample set. The heating efficiency was calculated by the following equation:

$$\eta = \frac{Q_{prod.}}{P_0(1 - 10^{-OD})} \quad (1)$$

where $Q_{prod.}$ is the photothermal heat power produced, P_0 is the irradiated power, and OD is at 808 nm. $Q_{prod.}$ was estimated from experimental cooling kinetics by means of:

$$Q_{prod.} = hA(T_{max.} - T_{amb.}) = \frac{\sum_i m_i c_{p,i}(T_{max.} - T_{amb.})}{\tau} \quad (2)$$

h and A being the heat transfer coefficient and the surface area for heat transfer to surroundings, respectively. $T_{max.}$ and $T_{amb.}$ are the maximum saturation temperature achieved during heating and the ambient temperature of surrounding area, respectively. In accordance with the literature, the product (hA) was estimated by summing the products of mass and specific heat capacities of the system components that dominate the heat exchange with AuBPs (i.e., solvent and cuvette), divided by the cooling time coefficients τ (Section S9, Supporting Information). The value of τ was estimated from the exponential fit of the cooling kinetics profile of each sample.

Figure 2f (dotted line) shows the variation of experimental heating efficiency with the sample volume, estimated through Equations (1) and (2) (Section S8, Supporting Information). We observed an increase in the photothermal heating efficiency (from ~50% to ~80%) when AuBP volumes decreased from 35431 to 7872 nm^3 (from AuBP6 to AuB2). This is due to the decreasing contribution of optical scattering to the extinction, where the scattered energy relaxes non-thermally, resulting in a loss of efficiency. Interestingly, we observed that the smallest AuBP exhibited a drop in the heating efficiency. This trend contradicts the numerical simulations, which predicted a monotonic increase in the heating efficiency with decreasing AuBP volumes (Figure 2d; Section S7, Supporting Information). We postulate that such a discrepancy is due to additional non-thermal relaxation pathways. It has been reported that for NPs with size smaller than 10 nm, the timescale for energy dissipation via phonon–phonon coupling becomes comparable to that of electron-phonon coupling.[18,33] This convergence in relaxation timescales may suggest that non-thermalized electrons can interact with the surrounding environment, introducing additional relaxation pathways and consequently reducing the photothermal heating efficiency of very small NPs. Furthermore, there appears to be a shape-dependent onset for these additional relaxation pathways, since in the previous works, Au nanorods with 15 nm in width (comparable to the width of smallest AuBP used in our study) do not show a similar loss of heating efficiency.[9,10] This is possibly due to the sharp tips of the bipyramids, the resulting local volume effect, and electric field enhancement caused by their large tip curvature (~1/r). Alternatively, the drop of efficiency at lower nanoparticles volume (larger number of nanoparticles) can be related to additional factors such as radiative heat transfer between particles or non-uniform temperature distribution in the medium.[30] Although the presence of such a shape dependence on non-thermal relaxation paths may explain the present results, further studies, including transient absorption measurements, theoretical and numerical calculations, are underway to shed full light on this effect.

2.3. Plasmonic Films Containing AuBPs

The exploitation of photothermal properties of AuNPs requires appropriate sample processing to meet the constrains imposed by specific applications. Put differently, transitioning from laboratory proof-of-concept experiments to real-world applications is a demanding process requiring adaptation of the sample to a targeted context. For example, optical hyperthermia used in clinics requires colloidally stable nanoparticles with biocompatible coating.[34] Solar-driven water desalination needs precisely assembled plasmonic Al nanoparticles on the walls of porous membranes to maximize broadband solar absorption.[35] Similarly, hydrogel monoliths featuring light-driven oscillatory movement need a rational distribution of nanoparticles within the polymer matrix.[36] Thus, only by placing the nanoparticles in the right context enables the exploitation of photothermal effect. Here, we aim to use the photothermal properties of AuBP to power a mechanical device (a Stirling engine, vide infra) which requires the use of nanoparticles in a solid state. Therefore, the structural constraints of the device necessitate a processable and robust thin film with optical properties similar to those in the colloidal phase, without compromising colloidal stability.

To meet these requirements, we developed a new method to embed AuBPs in agarose films (**Figure 3**). The CTAC-stabilized solutions of AuBP1 and AuBP6 (constant Au^0 concentration) were dispersed in a hot solution of low MW agarose and allowed to solidify in a custom-made silicon mold (see Section S1.5 and Video S1, Supporting Information). The combination of scanning electron microscopy and ion focused beam showed the mean thickness of the films to be 10 µm and uniform distribution of AuBPs throughout the polymer matrix (Figure 3a). The interparticle distance was (170 ± 73) nm (AuBP1) and (371 ± 132) nm (AuBP6), indicating that larger AuBPs are more sparsely distributed within the gel matrix (Figure 3a,b). Importantly, AuBPs retained their optical properties in the gel medium. The LSPR redshifted by ~74 nm, which is due to the change in the refractive index of the medium, from 1.333 (water) to 1.679 (agarose)[37,38] (Figure 3c). The linewidth of LSPR was conserved, confirming again the lack of aggregation.

To evaluate whether the plasmonic agarose films feature photothermal heating ability, we exposed the film to solar simulator irradiation (irradiance: 108 mW cm^{-2}, area: 16.24 cm^2 at a side length of 2.5 cm) by simultaneous monitoring the temperature change with a thermal camera. The intensity profile of incident light was adjusted to maximize the overlap with LSPR (Figure S7, Supporting Information). The plasmonic films generated a uniform temperature increase throughout the irradiated area, demonstrating their photothermal response even under light with relatively low power density compared to the laser system described above. Control experiments with bare agarose films showed negligible increase in temperature upon irradiation (Figure 3d). Furthermore, irradiation of the plasmonic films with increasing power led to a concomitant rise in temperature, ranging from 3.5 °C to 15 °C as the irradiation power increased from 37 to 108 mW cm^{-2} (Figure 3e). A detailed analysis of the heating response revealed that the slopes corresponding to AuBP1 and AuBP6 are comparable: 130 °C per W cm^{-2} for AuBP1 and 125 °C per W cm^{-2} for AuBP6. Additionally, the thermal conductivity of agarose[39] (0.121 W mK^{-1} at 37 °C for 4.5 wt%) is smaller

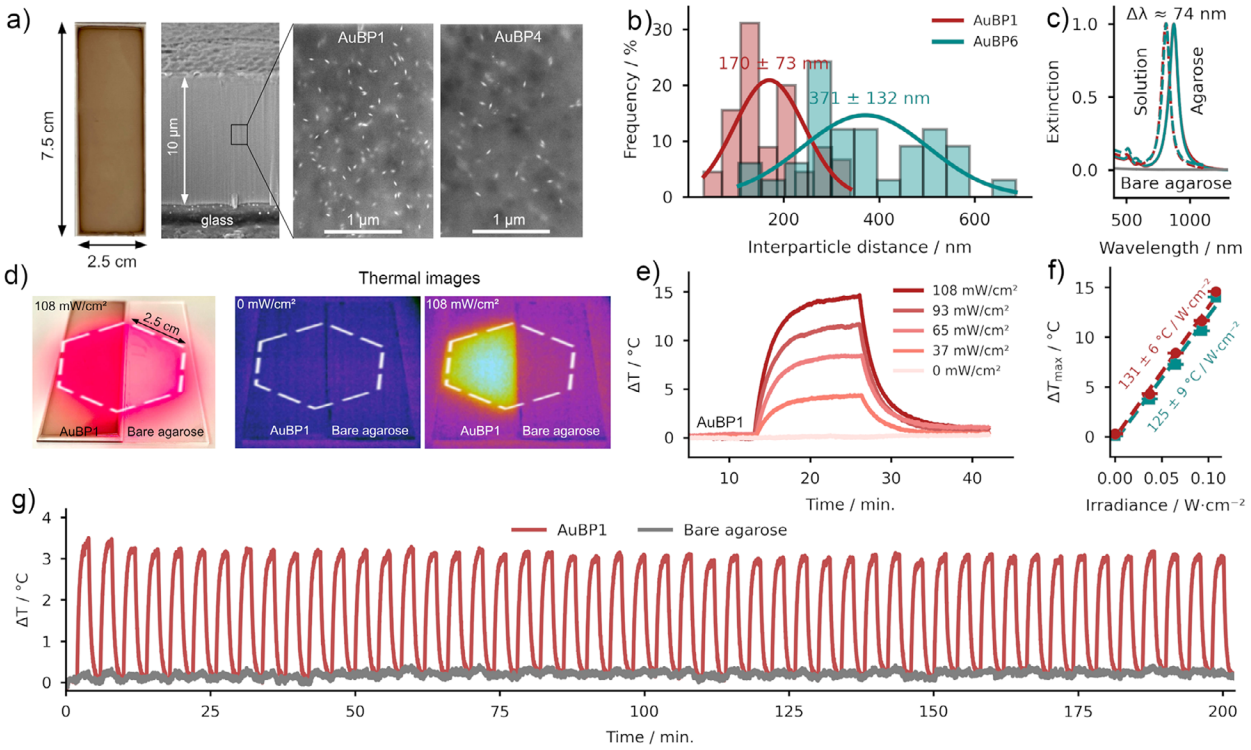

Figure 3. Plasmonic films containing AuBPs. a) Digital and SEM images of agarose films doped with AuBP1 and AuBP6. The dried film is 10 µ m thick. b) Mean interparticle distance within agarose film for AuBP1 and AuBP6. c) Normalized UV-Vis-NIR spectra of AuBP1 and AuBP6 in solution (dashed lines) and in dried agarose film (solid lines) showing ~ 74 nm redshift due to the change in the dielectric environment. d) Digital and thermal images of agarose films under dark and light conditions. e) Time-dependent temperature change for different power density of incident light. f) Maxima ΔT as a function of irradiance for AuBP1 and AuBP6. Dashed lines: linear fits. g) The long-term stability and response of the plasmonic film containing AuBP1 subjected to 50 cycles of light and dark periods (120 s each).

than the water thermal conductivity [40] (0.598 W mK^{-1}). This reduced thermal conductivity promotes heat retention within the agarose film, which explains the more pronounced temperature rise observed in the agarose films as compared to the temperature increase in dispersion ~ 4.7 °C. The photothermal conversion efficiencies calculated for plasmonic films incorporating AuBP1 and AuBP6 were determined to be 0.68 and 0.72, respectively (Table S7, Supporting Information). This observed difference between film samples mirrors the trend observed in nanoparticle dispersions, where corresponding values of 0.54 and 0.57 were obtained (Figure 2f). The elevated absolute values in the film configuration may be attributed, again, to thermal accumulation effects within the agarose matrix. Importantly, the estimated photothermal efficiency in the plasmonic film configuration provide further evidence for the presence of non-thermal relaxation pathways. These pathways appear to be associated with reduced particle volume and tip geometry, rather than being mediated by environmental factors. Finally, to assess the durability and stability of plasmonic films, we conducted a number of 50 heating-cooling cycles. To shorten the heating and cooling periods (2 min) the film was placed on a temperature controlled stage maintained at 20 °C. Upon irradiation with light by a solar simulator, the maximum temperature was ~3.2 °C, and consistently repeated over the entire experiment, demonstrating the robustness of photothermal performance. In summary, given the narrow and tunable plasmon band and the relatively high transmittance in the visible spectral range, our plasmonic films are promising candidates for infrared light harvesting system and associated heat management.

2.4. Powering Stirling Engine Through Wasted Heat

Finally, we investigated the photothermal ability of plasmonic films in enhancing the performance of a low-temperature differential Stirling engine through dissipated heat from plasmonic films.[41] Stirling engines operate by converting temperature differences (T_2-T_1) into mechanical work (rotating flywheel) via cyclic compression of a confined gas (**Figure** 4a). The expansion of gas upon heating pushes the displacer piston, then moves to the cooler side where it contracts, sustaining a cyclic expansion and compression process. This motion, maintained by the flywheel, efficiently converts thermal energy into mechanical work. The engine has a small compression ratio, a large displacer piston, and wide thermal conduction surfaces, optimizing low-temperature operation. The larger the temperature difference, the faster rotation of flywheel. Also, the direction of the thermal gradient determines the direction of the rotating flywheel.

In a typical experimental setup, the temperature values on both plates were monitored by thermocouples. A thermostat was used to maintain externally (a heat sink) the temperature of the

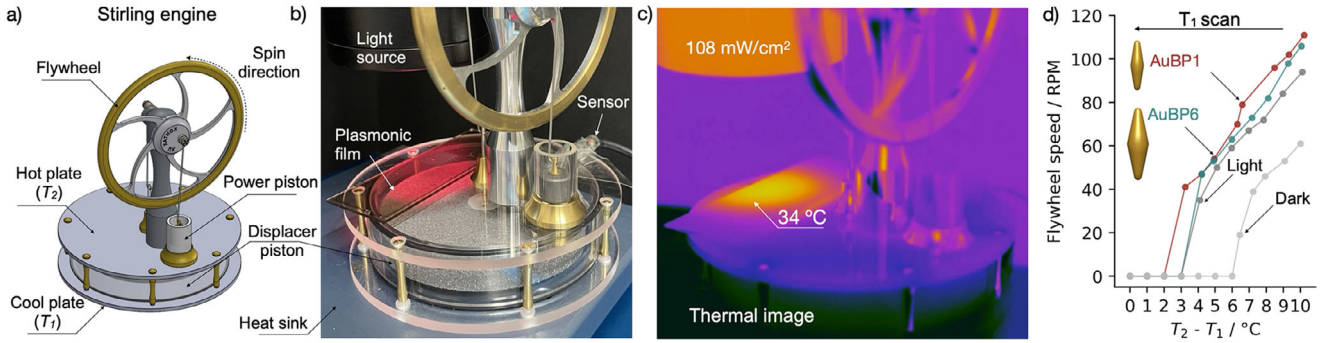

Figure 4. Plasmon-enhanced solar Stirling engine. a) Schematic diagram of Stirling engine. b) Digital photograph of experimental setup used to power Stirling engine under incident light. c) Thermal image of Stirling engine covered with plasmonic film under illumination. d) Revolutions per minutes of the flywheel as a function of temperature difference of upper and lower plates under dark and light condition and in the presence and absence of plasmonic film. The onset of temperature difference shifts toward lower values in the presence of plasmonic films indicating improved performance of Stirling engine. a) Reproduced with permission. Copyright Kontax Engineering Ltd 03/11/21.

lower plate in our Stirling engine (Figure 4b). The light was delivered from top by a solar simulator located at the distance of 7 cm. The light intensity profile was adjusted to maximize the overlap with LSPR of AuBPs (Figure S7, Supporting Information). The performance of Stirling engine was evaluated by tachometer application installed on a mobile phone (Section S1.2 and Video S2, Supporting Information) In a typical experiment, the initial temperature difference of 10 °C was progressively decreased by increasing the temperature of the lower plate in 1 °C intervals while monitoring in real time the flywheel revolutions per minute (rpm) in the anticlockwise direction.

Under dark conditions, the onset temperature difference to maintain the flywheel rotating was 6 °C that shifted further to 3 °C under light irradiation (108 mW cm^{-2}) (Figure 4d - grey lines). Upon irradiation, the displacer piston is heated by absorbed light, leading to a temperature difference within the chamber and thus improving the performance of the Stirling engine.

The presence of plasmonic films on the upper plate further increased the temperature difference and thus the performance of the engine. The photothermal response of the films resulted into a localized temperature increase, reaching 34 °C upon illumination (Figure 4c). For AuBP6, the values of rpm increased from ~94 to ~106 at 10 °C temperature difference, marking a 12.7% enhancement (red line in Figure 4d). The film containing AuBP1 displayed an even greater effect by increasing the rpm value to ~111, and reducing the onset temperature difference to 2 °C. The film containing AuBP1 showed 18% improvement in the performance as compared to light conditions without nanoparticles (Figure 4d - red line). Overall, our results demonstrate that by leveraging thermoplasmonic effects, we can increase the flywheel rpm values and lower the onset of temperature difference required to maintain its rotation. This also indicates that rational nanoscale photothermal engineering can enhance the performance of macroscopic devices powered by '*wasted heat*'.

3. Conclusion

The present study provides a comprehensive experimental analysis of size-dependent photothermal heating efficiencies of anisotropic nanoparticles. We used AuBP samples with 5.2-fold variation in volume while maintaining constant aspect ratios and invariant position of LSPR at 808 nm. By confirming a commonly accepted behavior, we found that the trend of photothermal heating on individual nanoparticles is proportional to the nanoparticle volume since nanoparticles of larger volumes are better light absorbers. The trend reversed at the multi-particle system, especially in terms of photothermal heating performance. The larger AuBPs exhibited lower efficiencies due to increased scattering contributions. Interestingly, contrary to conventional expectations, the smallest *absorption-dominant* AuBPs, too, showed reduced photothermal efficiencies. We attribute this behavior to the potential onset of additional relaxation pathways. Indeed, we foresee the need for further investigation using techniques like ultrafast transient absorption spectroscopy and detailed theoretical models. Finally, we demonstrated the practical implications of the photothermal heating abilities of AuBPs by generating temperature differences that can drive a Stirling engine. This tangible demonstration highlights the potential of AuBPs for applications in thermoplasmonic devices. By systematically exploring the interplay between size and photothermal efficiency in AuBPs, this work expands the understanding of anisotropic NPs behavior. It also lays the groundwork for optimizing their geometric and optical properties for applications in advanced sensing, catalysis, and energy technologies.

Supporting Information

Supporting Information is available from the Wiley Online Library or from the author.

Acknowledgements

This work was supported by the grant PID2022-141017OB-I00 funded by MCIN/ AEI/10.13039/ 501100011033 and by "ERDF A way of making Europe". A.R. acknowledges funding from the Spanish MICIU for the Juan de la Cierva (FJC2021-047710-I) fellowship. J. L., M.-P., and A.S.-I acknowledge the financial support received from the IKUR Strategy under the collaboration agreement between the Ikerbasque Foundation and Materials Physics Center on behalf of the Department of Science, Universities and Innovation of the Basque Government. This work was partially supported by the Croatian Science Foundation under project number HRZZ-IP-2022-10-3456, which S.A.M., M.G., and J.S.P. acknowledge. N.M.D acknowledges

the support of AI & GAMING EDIH project funded through Digital Europe Programme, grant 101083963. The authors thank Andrey Chuvilin (CIC nanoGUNE BRTA) for SEM characterization of plasmonic films.

Conflict of Interest

The authors declare no conflict of interest.

Data Availability Statement

The data that support the findings of this study are available from the corresponding author upon reasonable request.

Keywords

gold bipyramids, photothermal heating, plasmonic films, stirling engine, thermoplasmonics

Received: March 29, 2025
Revised: June 10, 2025
Published online: July 18, 2025

[1] A. Boltasseva, H. A. Atwater, *Science* **2011**, *331*, 290.
[2] J. C. Ndukaife, V. M. Shalaev, A. Boltasseva, *Science* **2016**, *351*, 334.
[3] Y. Ren, Q. Chen, M. He, X. Zhang, H. Qi, Y. Yan, *ACS Nano* **2021**, *15*, 6105.
[4] M. Overchuk, R. A. Weersink, B. C. Wilson, G. Zheng, *ACS Nano* **2023**, *17*, 7979.
[5] A. Lenert, D. M. Bierman, Y. Nam, W. R. Chan, I. Celanović, M. Soljačić, E. N. Wang, *Nature Nanotechnol.* **2014**, *9*, 126.
[6] R. K. Kashyap, P. P. Pillai, *Nano Lett.* **2024**, *24*, 5585.
[7] H. Zhang, H. Zeng, A. Eklund, H. Guo, A. Priimagi, O. Ikkala, *Nat. Nanotechnol.* **2022**, *17*, 1303.
[8] A. Paściak, A. Pilch-Wróbel, Ł. Marciniak, P. J. Schuck, A. Bednarkiewicz, *ACS Appl. Mater. Interfaces* **2021**, *13*, 44556.
[9] M. A. Mackey, M. R. Ali, L. A. Austin, R. D. Near, M. A. El-Sayed, *J. Phys. Chem. B* **2014**, *118*, 1319.
[10] S. M. Meyer, J. Pettine, D. J. Nesbitt, C. J. Murphy, *J. Phys. Chem. C* **2021**, *125*, 16268.
[11] J. R. Cole, N. A. Mirin, M. W. Knight, G. P. Goodrich, N. J. Halas, *J. Phys. Chem. C* **2009**, *113*, 12090.
[12] G. Baffou, R. Quidant, C. Girard, *Appl. Phys. Lett.* **2009**, *94*, 15.
[13] A. T. Diallo, M. Tlemçani, M. Khan, J. Spadavecchia, N. Djaker, *Part. Syst. Charact.* **2020**, *37*, 2000255.
[14] A. Paściak, R. Marin, L. Abiven, A. Pilch-Wróbel, M. Misiak, W. Xu, K. Prorok, O. Bezkrovnyi, U. Marciniak, C. Chanéac, F. Gazeau, R. Bazzi, S. Roux, B. Viana, V.-P. Lehto, D. Jaque, A. Bednarkiewicz, *ACS Appl. Mater. Interfaces* **2022**, *14*, 33555.
[15] Z. Qin, Y. Wang, J. Randrianalisoa, V. Raeesi, W. C. Chan, W. Lipiński, J. C. Bischof, *Sci. Rep.* **2016**, *6*, 29836.
[16] H. Chen, L. Shao, T. Ming, Z. Sun, C. Zhao, B. Yang, J. Wang, *Small* **2010**, *6*, 2272.
[17] H. Petrova, M. Hu, G. V. Hartland, *Z. Phys. Chem.* **2007**, *221*, 361.
[18] G. V. Hartland, *Chem. Rev.* **2011**, *111*, 3858.
[19] K. Jiang, D. A. Smith, A. Pinchuk, *J. Phys. Chem. C* **2013**, *117*, 27073.
[20] Q. Li, X. Zhuo, S. Li, Q. Ruan, Q.-H. Xu, J. Wang, *Adv. Opt. Mater.* **2015**, *3*, 801.
[21] Y. Ni, C. Kan, J. Xu, *Phys. Chem. Chem. Phys.* **2022**, *24*, 21522.
[22] T. H. Chow, N. Li, X. Bai, X. Zhuo, L. Shao, J. Wang, *Acc. Chem. Res.* **2019**, *52*, 2136.
[23] A. Sánchez-Iglesias, N. Winckelmans, T. Altantzis, S. Bals, M. Grzelczak, L. M. Liz-Marzán, *J. Am. Chem. Soc.* **2017**, *139*, 107.
[24] A. Sánchez-Iglesias, M. Grzelczak, *Small* **2024**, 2407735.
[25] J. L. Montaño-Priede, A. Sánchez-Iglesias, S. A. Mezzasalma, J. Sancho-Parramon, M. Grzelczak, *J. Phys. Chem. Lett.* **2024**, *15*, 3914.
[26] U. Hohenester, A. Trügler, *Comput. Phys. Commun.* **2012**, *183*, 370.
[27] P. B. Johnson, R. W. Christy, *Phys. Rev. B* **1972**, *6*, 4370.
[28] G. Baffou, *Thermoplasmonics: Heating Metal Nanoparticles Using Light*, Cambridge University Press **2017**, pp. 81–100.
[29] M. Quintanilla, C. Kuttner, J. D. Smith, A. Seifert, S. E. Skrabalak, L. M. Liz-Marzán, *Nanoscale* **2019**, *11*, 19561.
[30] H. Zhang, H.-J. Chen, X. Du, D. Wen, *Sol. Energy* **2014**, *100*, 141.
[31] D. K. Roper, W. Ahn, M. Hoepfner, *J. Phys. Chem. C* **2007**, *111*, 3636.
[32] A. R. McCluskey, *J. Chem. Educ.* **2023**, *100*, 4174.
[33] M. Hu, G. V. Hartland, *J Phys. Chem. B* **2002**, *106*, 7029.
[34] A. R. Rastinehad, H. Anastos, E. Wajswol, J. S. Winoker, J. P. Sfakianos, S. K. Doppalapudi, M. R. Carrick, C. J. Knauer, B. Taouli, S. C. Lewis, A. K. Tewari, J. A. Schwartz, S. E. Canfield, A. K. George, J. L. West, N. J. Halas, *Proc. Natl. Acad. Sci.* **2019**, *116*, 18590.
[35] L. Zhou, Y. Tan, J. Wang, W. Xu, Y. Yuan, W. Cai, S. Zhu, J. Zhu, *Nat. Phot.* **2016**, *10*, 393.
[36] Y. Zhao, C. Xuan, X. Qian, Y. Alsaid, M. Hua, L. Jin, X. He, *Sci. Robot.* **2019**, *4*, eaax7112.
[37] K. L. Kelly, E. Coronado, L. L. Zhao, G. C. Schatz, *J. Phys. Chem. B* **2003**, *107*, 668.
[38] ChemBK, Agarose, **n.d.**, https://www.chembk.com/en/chem/Agarose, Accessed: 2025-03-11.
[39] E. Myers, M. Piazza, M. Owkes, R. K. June, *J. Biomech.* **2024**, *176*, 112307.
[40] M. Ramires, C. Nieto de Castro, Y. Nagasaka, A. Nagashima, M. Assael, W. Wakeham, *J. Phys. Chem. Ref. Data* **1995**, *24*, 1377.
[41] Y. Izumida, *Europhys. Lett.* **2018**, *121*, 50004.